Highly Transparent Fluorotellurite Glass-Ceramics: Structural Investigations and Luminescence Properties

Jean-Paul Laval, Jean-René Duclère, Vincent Couderc, Mathieu Allix, Cécile Genevois, Vincent Sarou-Kanian, Franck Fayon, Pierre-Eugène Coulon, Sébastien Chenu, Maggy Dutreilh-Colas, et al.

Highly transparent fluorotellurite glass-ceramics: structural investigations and luminescence properties

Jean-Paul Laval[1], Jean-René Duclère[1], Vincent Couderc[2], Mathieu Allix[3], Cécile Genevois[3], Vincent Sarou-Kanian[3], Franck Fayon[3], Pierre-Eugène Coulon[4], Sébastien Chenu[1], Maggy Colas[1], Julie Cornette[1], Philippe Thomas[1], Gaëlle Delaizir[1*]

[1]*Institut de Recherche sur les Céramiques (IRCER), UMR 7315 CNRS, Université de Limoges, Centre Européen de la Céramique, Limoges, France*

[2]*Xlim, UMR 7252 CNRS, Université de Limoges, France*

[3]*Conditions Extrêmes et Matériaux : Haute Température et Irradiation (CEMHTI), UPR3079 CNRS, Orléans, France*

[4]*Laboratoire des Solides Irradiés, Ecole Polytechnique, Palaiseau, France*

*Corresponding author: gaelle.delaizir@unilim.fr

Abstract

Crystallization from glass can lead to the stabilization of metastable crystalline phases, which offers an interesting way to unveil novel binary or ternary compounds and control the optical properties of obtained glass-ceramics. Here, we report on a crystallization study of the ZrF_4-TeO_2 glass system and show that under specific synthesis conditions, a previously unreported $Zr_{10}Te_9O_xF_y$ zirconium oxyfluorotellurite anti-glass phase can be selectively crystallized at the nanometric scale within the $65TeO_2$-$35ZrF_4$ amorphous matrix. This leads to highly transparent glass-ceramics in both the visible and near infrared ranges. Under longer heat-treatment, the stable cubic $ZrTe_3O_8$ phase crystallizes in addition to the previous unreported anti-glass phase. The structure, microstructure and optical properties of different $65TeO_2$-$35ZrF_4$ Tm^{3+}-doped glass-ceramics, were investigated in detail by means of X-ray diffraction,

scanning and transmission electron microscopies, ^{19}F, ^{91}Zr and ^{125}Te NMR, Raman and photoluminescence spectroscopies.

Single crystals of this novel phase could be successfully synthesized from the liquid state and their basic structure has been determined. The crystal chemistry study of several samples evidences various superstructures along a, b and c axes and likely twinning of crystals, suggesting that the novel phase corresponds to a complex series of micro-phases rather than a stoichiometric compound. These results highlight the peculiar disorder-order phenomenon occurring in tellurite materials.

Introduction

Due to their large optical window extending in the infrared range up to 5 µm, tellurite glasses can be used as optical laser fiber devices.[1-3] Among their remarkable properties, their high linear and nonlinear refractive indices enable photonic applications (ex: supercontinuum generation, optical switches, etc).[4,5] Further, tellurite fibers could be attractive candidates for spatial beam self-cleaning in multimode fibers able to produce powerful laser source oscillating on a single spatial transverse mode.[6] The main drawback of these materials remains their high hydroxyl group content which is detrimental to exploit the intrinsic mid-infrared transparency of tellurite glass fibers, thus efforts have been focused on this critical point during the last decades.[7-11]

Tellurite and fluorotellurite glass-ceramics have driven interest as these materials can stabilize non-centrosymmetric crystalline phases that are a key focus in nonlinear optics, especially for the generation of second harmonic.[12,13] The presence of nanocrystals, that are small enough to prevent light scattering, allows rare earth or transition metal ions to incorporate into a

crystalline fluoride phase is a prominent criterion to develop efficiency of oxyfluorotellurite transparent glass-ceramics as active hosts.[14-18]

Here, we report on a systematic investigation of the synthesis and crystallization of glasses in the ZrF_4-TeO_2 system. This system, part of a quaternary Zr-Te-O-F system, was likely to present vitreous domains, as the well-known fluorozirconate glasses, the tellurite glasses and the oxyfluorotellurite glass domain already investigated in the binary TeO_2-TeF_4, near TeF_4.[19] The ZrF_4-TeO_2 system exhibits a limited vitreous domain leading to a few choices of glass compositions. Interestingly, we show that a novel and unreported phase can be selectively crystallized within the specific $65TeO_2$-$35ZrF_4$ glassy matrix by controlling the thermal treatment of the parent glass. This peculiar and soft devitrification process is a powerful tool to produce such novel phases.[20-22] The new phase is in fact an anti-glass also called "glass of anions". This concept was first introduced by Trömel *et al.* in 1983.[23] An anti-glass is defined as a solid material with a clear cationic long range-order (hence the existence of Bragg peaks in X-ray diffraction patterns) but without any anionic long range order (thus, the observed Raman signature is similar to that of glass materials). There is therefore a peculiar and interesting order/disorder coexistence in such materials. Only a few anti-glass structures have been reported up to now. These are based on the CaF_2 fluorite structure with Te^{4+} and metal ions statistically distributed in the cationic positions and with the anionic crystallographic positions not fully occupied. As previously mentioned, anti-glass materials are also called "glasses of anion" in reference to the disorder on anion sites. Among reported anti-glasses, $SrTe_5O_{11}$, $Ln_2Te_6O_{15}$, $Ln_2Te_6O_{11}$, $Bi_2Te_4O_{11}$, $Bi_{0.5}Nb_{0.5}Te_3O_8$ and $Bi_{0.8}Nb_{0.8}Te_3O_8$ materials can be cited.[24-28]

The resulting $65TeO_2$-$35ZrF_4$ glass-ceramics are highly transparent due to the presence of nanocrystals even when stabilizing two different crystalline phases *i.e* the unreported anti-glass and the cubic $ZrTe_3O_8$ phases while maintaining very low hydroxyls groups content due

to the presence of fluorine in the composition. These glass-ceramics have been investigated in details by means of X-ray diffraction, ^{19}F, ^{91}Zr and ^{125}Te NMR, Raman spectroscopy, scanning and transmission electron microscopies. Since there is limited number of reports on the tellurite based glass-ceramics containing oxyfluoride nanocrystals doped with rare-earth ions, the luminescence of Tm^{3+}-doped glass-ceramics has also been studied in both the visible and near-infrared ranges.

To go further in the structural determination of this novel $Zr_{10}Te_9O_xF_y$ crystalline phase corresponding to an anti-glass, further synthesis experiments have been conducted in order to obtain single crystals. Slow cooling from the liquid state of different compositions in the TeO_2-ZrF_4 binary system has been used leading to micrometer scale single crystals that exhibit superstructures and twins as evidenced by single-crystal X-Ray diffraction. This result evidences the complex order/disorder phenomena taking place in these oxyfluorotellurite crystals that is discussed in the present paper.

Experimental section

Syntheses. The glass forming domain of the TeO_2-ZrF_4 system was determined using 2g of the different stoichiometric compositions $xZrF_4$-$(1-x)TeO_2$ (with $0<x<1$) that were synthesized from starting elements ZrF_4 (Strem Chemicals, 99.9%) and TeO_2 (Alfa Aesar, 99.99%). The mixtures have been heated up to 850°C in a covered platinum crucible, stirred twice and then quenched by pouring the high temperature melt between two metallic plates.

Glasses with nominal composition $65TeO_2$-$35ZrF_4$ (with or without 1% at. Tm^{3+} doping content introduced as TmF_3) were synthesized as described above but in order to obtain glass bulks, an annealing treatment was performed at Tg-10°C after the quenching step in order to relax the mechanical constraints in the glass.

Glass-ceramics were synthesized by heating the $65TeO_2$-$35ZrF_4$ parent glass at 340°C for different durations (from 30 min to 3h).

Single crystals of the novel phase were prepared from compositions in the range $40ZrF_4$-$60TeO_2$ to $50ZrF_4$-$50TeO_2$. 2 g of stoichiometric compositions were melted at 800°C in a covered platinum crucible and slowly cooled down to 600°C, 500°C or 400°C and then quenched in air in order to understand the order/disorder phenomena related to this new crystalline phase.

Structural, microstructural and chemical characterizations. To check the amorphous nature of the samples and to identify the crystalline phases, X-Ray Diffraction (XRD) measurements were carried out at room temperature using a D8 Advance Bruker diffractometer equipped with a primary monochromator, a fast Lynxeye detector and CuKα1 radiation (λ_{Cu}=1.5406 Å) on the surface of the glass and glass-ceramic bulk samples.

The diffraction patterns of single crystals were recorded on a 4-circle Nonius diffractometer equipped with a graphite monochromator and a CCD camera. Data collection and reduction were performed with the program suite COLLECT, DIRAX/LSQ and EVALCCD.

High resolution Transmission Electron Microscopy (HR-TEM) and Selected Area Electron Diffraction (SAED) were performed on a JEOL 2010F operating at 200 kV and having a point-to-point resolution of 2.3 Å. Scanning Transmission Electron Microscopy - High Angle Annular Dark Field (STEM-HAADF) imaging, Energy Dispersive X-ray Spectroscopy (EDX) mapping and Energy Filtered Transmission Electron Microscopy (EFTEM) imaging were obtained using a JEOL ARM200F (JEOL Ltd.) cold FEG operating at 120 kV, equipped with a double spherical aberration correctors and fitted with a JEOL SDD CENTURIO EDS system and a GIF Quantum. For EDX map and STEM-HAADF image, a 0.13 and 0.1 nm probe size were used respectively. The glass-ceramics (1h30 and 2h heat-treatments) were

prepared prior to (S)TEM observations by Focused Ion Beam (FIB, FEI Scios). Compositions of the parent glass and single crystals were estimated using Energy Dispersive X-Ray Spectroscopy (EDX-SEM, JEOL IT 300).

Raman spectroscopy experiments on the $65TeO_2$-$35ZrF_4$ glass and corresponding glass-ceramics were performed using an In Via Reflex Renishaw Raman spectrophotometer. The spectra were recorded using a x50 objective and a 532 nm wavelength excitation with a power of 40 mW.

The thermal behavior of the as-quenched samples was studied by Differential Scanning Calorimetry (DSC) performed using TA instrument AQ100 equipment from 300 up to 723 K and using a heating rate of 10 $K.min^{-1}$.

^{19}F and ^{125}Te solid-state nuclear magnetic resonance (NMR) experiments were performed on a Bruker Avance III HD spectrometer operating at 4.7 T (Larmor frequencies of 188.33 MHz and 63.24 MHz for ^{19}F and ^{125}Te, respectively) using 4 mm and 1.3 mm magic angle sample spinning (MAS) double-resonance probeheads. Quantitative ^{125}Te MAS and ^{125}Te-{^{19}F} cross-polarization (CP) MAS spectra were recorded at a spinning frequency of 14.285 kHz using a spin-echo sequence (echo delay of 140 µs) and ^{19}F high-power decoupling. The recycle delay was set to 90 s for direct excitation and 13 s for CP experiment (contact time of 3ms). Quantitative ^{19}F spin-echo MAS spectra were recorded at a spinning frequency of 60 kHz with a recycle delay of 60 s. 1D and 2D ^{19}F-{^{125}Te} Heteronuclear Single Quantum Correlation (HSQC) MAS spectra allowing to probe F-Te bonding were recorded at a spinning frequency of 60 kHz.[29] Under such fast sample spinning, the coherence transfer is expected to be driven by isotropic ^{19}F-{^{125}Te} *J*-couplings and the best-efficiency was achieved using excitation and reconversion delays of 133 µs. ^{19}F {^{91}Zr}-dephased MAS spectra were recorded using a ^{19}F spin-echo sequence with a ^{91}Zr Phase-Modulated Low-Alpha/Low-Amplitude (PM-LA) pulse applied in the middle of the echo period, such that ^{19}F

dephasing occurs due to ^{19}F-^{91}Zr isotropic *J*-couplings and second-order dipolar-quadrupolar effects.[30] Sample spinning rate of 50 kHz and dephasing time of 2.2 ms were used. ^{19}F homonuclear dipolar double-quantum (DQ) correlation experiment allowing to probe F-F proximities were performed at a spinning frequency of 50 kHz using the SPIP recoupling sequence.[31] DQ excitation and reconversion period were set to 150 µs. For the ^{19}F-{^{125}Te}, ^{19}F-{^{91}Zr} double-resonance and ^{19}F double-quantum experiment the recycle delay was set to 13 s. ^{125}Te and ^{19}F chemical shifts were referenced relative to $Te(CH_3)_2$ and $CFCl_3$, respectively, using diphenyl ditelluride dissolved in $CDCl_3$ (δ= -422 ppm) and 4'-fluoroacetone (δ= -107 ppm) as secondary references.

Optical measurements. UV-visible-Near InfraRed (NIR) optical transmission measurements of polished Tm^{3+}-doped samples (glass and glass-ceramics) were carried out in the 200 – 3300 nm range, under normal incidence, using a Varian Cary 5000 spectrophotometer operated in dual beam configuration.

Complete refractive index dispersion curves were measured by spectroscopic ellipsometry (Horiba Jobin–Yvon UVISEL), operated at a fixed 65° incidence angle (close to the Brewster's angle). However, only the refractive index at infinite wavelength is reported.

Room temperature visible photoluminescence (PL) properties were measured using a Horiba-Jobin-Yvon Fluorolog 3 spectrofluorimeter, operated in reflective geometry. For the recorded phosphorescence emission spectra, the data step was fixed to 1 nm. In order to completely get rid of any residual excitation pulse stray light, PL decay curves were measured by setting an initial delay of 50 µs and with time interval steps of 5 µs.

Fluorescence measurements in the near infrared domain were realized in transmission mode by illuminating the different samples (glass and glass-ceramics) with a multimode beam operating at 808 nm and delivered by a fibered laser diode. The incident light was focused by

using convergent lens in order to reach a high power pump density. The detection of the fluorescence was realized by an optical spectrum analyzer (Yokogawa AQ6376) connected to a 400 µm core multimode fiber able to guide the infrared wavelengths up to 2.4 µm.

Results and discussion

Thermal properties of parent glasses. The glass forming domain in the ZrF_4-TeO_2 system has been determined in the present study by melting 2g of each composition at 850°C in a platinum crucible and quenching the liquid between two stainless steel plates. The domain is shown in Figure 1. The vitreous domain extends from $55TeO_2$-$45ZrF_4$ to $85TeO_2$-$15ZrF_4$ (mol %). These glasses are stable and non-hygroscopic at ambient conditions.

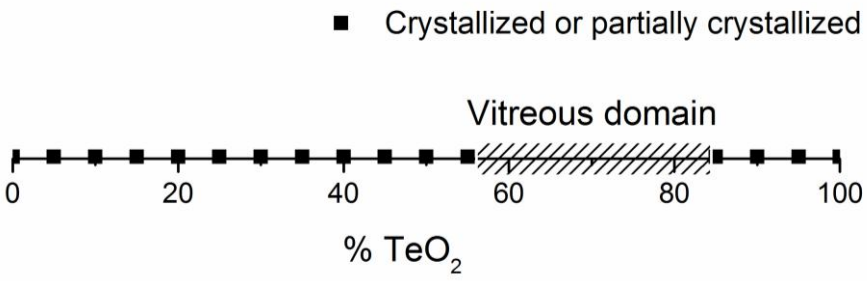

Figure 1: Vitreous domain in the (100-x)ZrF_4-xTeO_2 system (0<x<100)

From these results, the composition $65TeO_2$-$35ZrF_4$ was chosen to further elaborate glass-ceramic materials. This specific composition was investigated since i) it is rich in ZrF_4 and the chance to crystallize the well-known but unwanted α-TeO_2 is minimum, ii) the glass is thermally stable enough to prepare 8 mm diameter glass bulks. The DSC thermogram recorded with a heating rate of 10 $K.min^{-1}$ of this glass composition doped with 1% Tm^{3+} is shown in Figure 2. The glass transition temperature T_g and the glass stability, evaluated by the Dietzel criterion $\Delta T = T_c - T_g$ where T_c is the temperature of the onset of the first crystallization

peak, are 303 °C and ΔT = 63°C respectively. It is noteworthy that the addition of 1% at. of TmF_3 to the initial composition does not lead to any change in the temperature of glass transition T_g but shifts the temperature of crystallization temperature T_{c1} to lower temperature (~10°C) in comparison to the undoped glass. A second crystallization peak is observed at T_{c2} ~ 440°C. The thermograms obtained from bulk or powdered samples are quite similar in curve shape and we can also notice a shift of ~ 20°C in the temperature of first crystallization T_{c1} between powdered and bulk samples. This suggests a competition between bulk nucleation that is more willing to lead to optical transparent glass-ceramics and surface crystallization. The theoretical and experimental $65TeO_2$-$35ZrF_4$ parent glass compositions have been compared by EDS-SEM experiments and the values of the ratio Te/Zr (at. %) are 1.86 and 1.55 respectively, evidencing some chemical losses during the glass elaboration. Even if the synthesis was performed using a covered platinum crucible, limited evaporation (mainly of ZrF_4 since this compound exhibits low boiling point) took place during the glass synthesis.

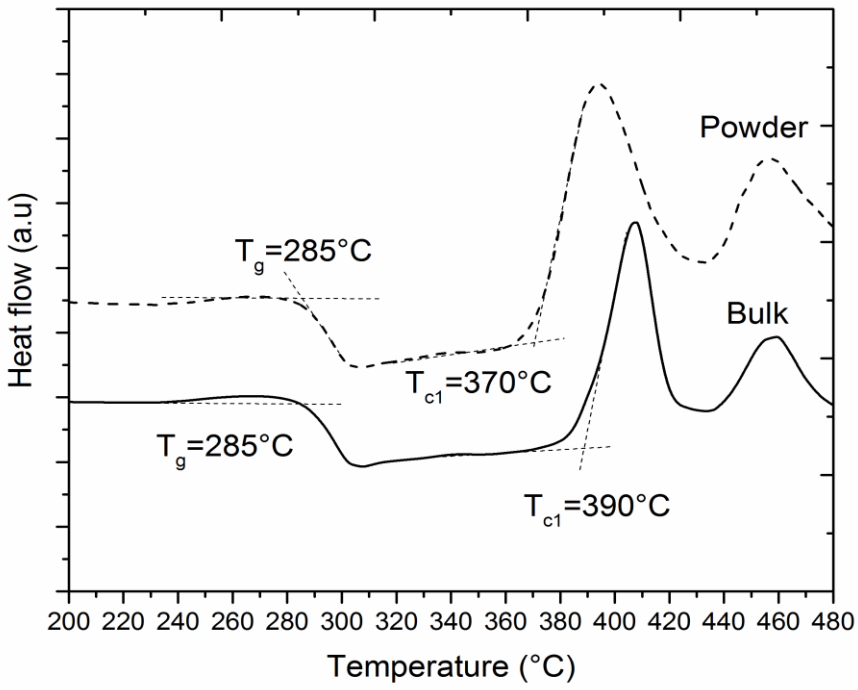

Figure 2: DSC thermograms of the $65TeO_2$-$35ZrF_4$ (doped with 1% at Tm^{3+}) glass composition

Based on the crystallization behavior determined by DSC data, we carried out a series of heat-treatments on this $65TeO_2$-$35ZrF_4$ glass composition. The temperature and dwell time were the adjustable parameters. Different glass-ceramics were prepared with a single heat-treatment (nucleation and growth at the same temperature) at 340°C during times ranging from 30 minutes to 3 hours. The single heat-treatment (rather than the two-step heat-treatment) was motivated by the structural study that is more focused on the stabilization of new crystalline phases rather than the control of the glass-ceramic microstructure.

Characterizations of $65TeO_2$-$35ZrF_4$ glass-ceramics. *a. Structural and microstructural characterizations.* The amorphous nature of the samples after synthesis by melt-quenching and the nature of the phases crystallizing in the glass matrix after heat-treatment at 340°C for different durations were determined by XRD measurements (Figure 3).

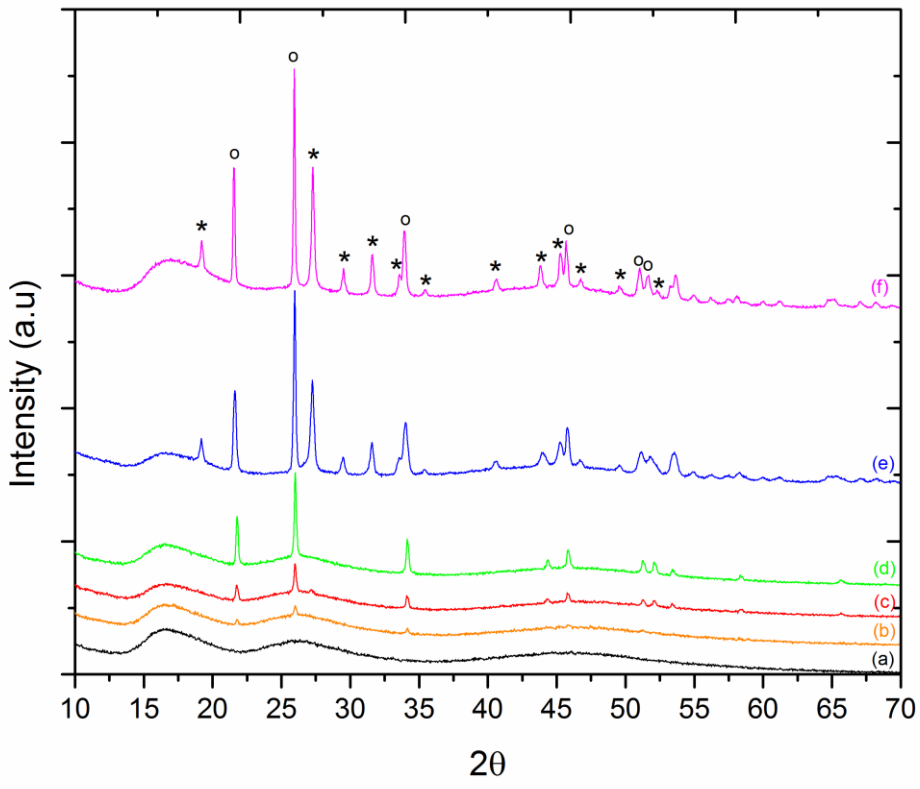

Figure 3: XRD patterns of the Tm^{3+}-doped $65TeO_2$-$35ZrF_4$ glass (a) and the corresponding glass-ceramics prepared at 340°C with the durations: 30 min (b), 1 h (c), 1h30 (d), 2 h (e), 3h (f). The symbols correspond to the crystalline phases: ○ new phase, ✶ $ZrTe_3O_8$.

The well-defined diffraction peaks that show up in the $65TeO_2$-$35ZrF_4$ based glass-ceramics (from a 30 min heat-treatment) correspond to the signature of an unreported crystalline phase which can be indexed in the hexagonal/trigonal system with the lattice parameters: a~3.9 Å and c~4.02 Å. Such a finding led us to investigate the direct synthesis of this novel crystalline phase, never reported earlier. A partial resolution of its crystal structure is reported later in the present article. When the heat-treatment of the $65TeO_2$-$35ZrF_4$ glass is longer than 2 hours (at 340°C), a secondary phase corresponding to a well-known cubic and derived fluorite-type

structure $ZrTe_3O_8$ is appearing. We stipulate that the high temperature DSC peak should thus be attributed to this latter phase.

To go further in the structural characterizations, Raman spectroscopy data were also collected. Raman spectra were recorded on the parent glass ($65TeO_2$-$35ZrF_4$ composition) and related glass-ceramic (heat-treatments of 1h30, 2h and 3h at 340°C) materials (Figure 4). One can first observe that the Raman bands are rather broad (as broad as for the initial glass) in the case of the 1h30 glass-ceramic sample. This experimental observation reflects the existence of structural disorder at short (wide distribution of Te-O and Zr-F(O) distances) and medium ranges, in the case of this specific glass-ceramic, thus, proving the "anti-glass" nature of the unreported detected crystal phase. The good stability of the parent glass and the corresponding glass-ceramics excludes the presence of Te-F bonds, as already observed for oxyflurotellurite crystals.[19] The band at around 450 cm^{-1} can be assigned to symmetric stretching vibrations of Te-O-Te (Zr) or O-Te(Zr)-O(F) bridges. The bands at 680 cm^{-1}, 790 cm^{-1} and 860 cm^{-1} are attributed to the stretching mode of trigonal bipyramid TeO_4 units, to the stretching vibrations of trigonal pyramidal TeO_3 and TeO_{3+1} units with non-bridging oxygens (NBO) and asymmetric vibrations of Te-O-Zr (Te) bondings respectively. Note that some oxygens may be replaced by two fluorine atoms breaking the former network. Since the Raman vibrations are mainly sensitive to the polarizability of the tellurium entities, the change induced by a likely formation of oxyfluoride tellurite entities should affect the Raman spectrum feature. These probable substitutions are not obvious and remain soft, their signature being hidden within the broad band 600-800 cm^{-1}.[32]

The Raman spectra of the samples heated for 2h or 3h at 340°C (Figure 4) are characteristics of crystalline materials as they exhibit several and well defined bands. The attribution of the main bands is compatible with the cubic $ZrTe_3O_8$ crystalline phase.[33,34]

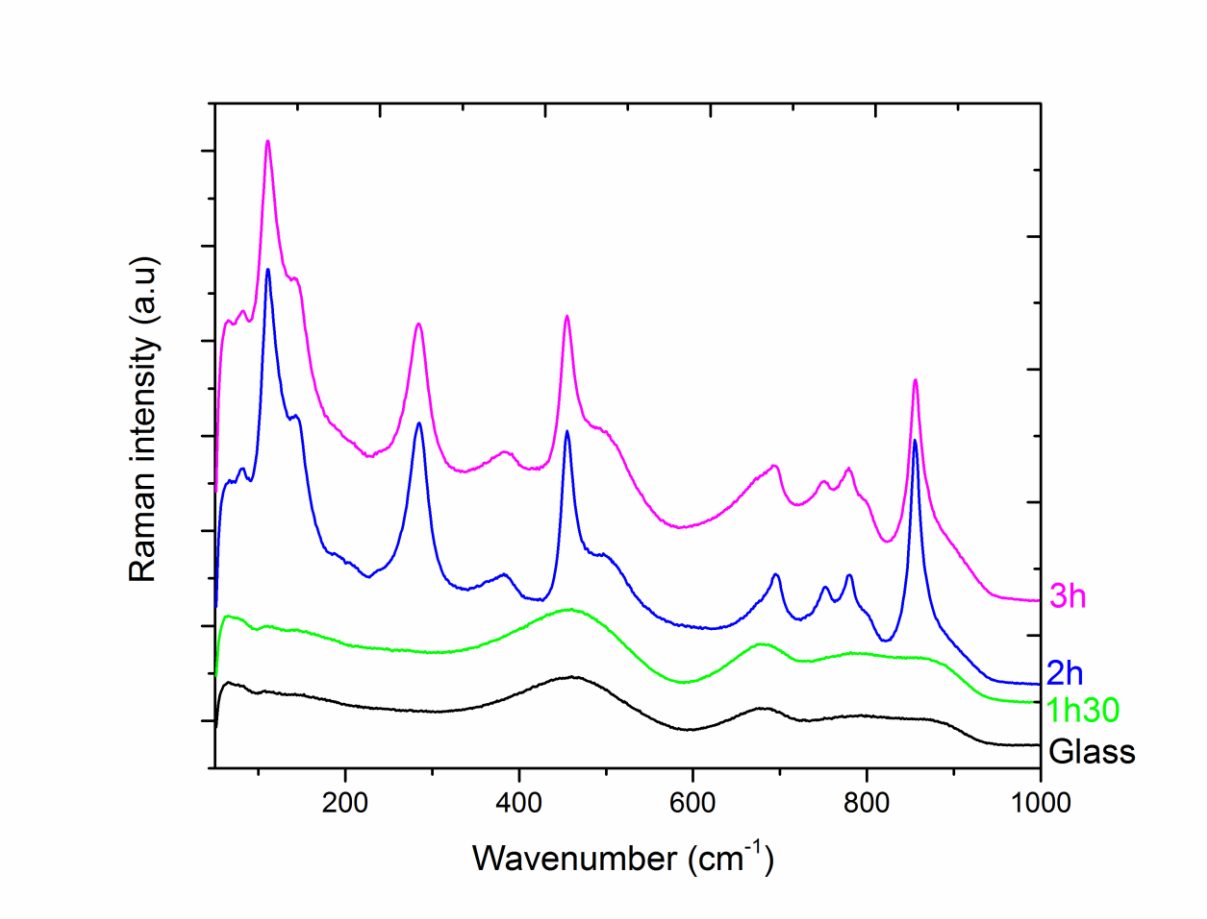

Figure 4: Raman spectra of the parent glass and its corresponding glass-ceramics heat-treated at 340°C for different durations

Figures 5 and 6 show STEM-HAADF and HRTEM images of the two glass-ceramics (1h30 and 2h of heat-treatment at 340°C) evidencing different nanostructures. The ~ 100 nm crystals of the novel anti-glass phase in the 1h30 glass-ceramic exhibit "butterfly wings"-like or hexagonal microstructures (depending on their orientation relative to the electron beam) (Figure 5). As shown by SAED patterns, the hexagonal or butterfly-like microstructures correspond to the same anti-glass phase. In Figure 5(b), the [101] direction of the new hexagonal anti-glass phase (a=3.9Å, c=4.02Å) is evidenced while in Figure 5(c) corresponds to the [001] direction.

EDX-TEM analysis revealed that the $65TeO_2$-$35ZrF_4$ based glass-ceramic contains crystals enriched in Zr and F as evidenced by Zr and Te EDX maps and fluorine EFTEM map with the approximatively $Zr_{10}Te_9O_xF_y$ composition (ratio Zr/Te=1.1) (Figure 5d). F and O are light chemical elements therefore their analysis is quite difficult with high uncertainties. In fact, this new phase does not belong to the pseudo-binary ZrF_4-TeO_2 system but rather to the quaternary ZrF_4-TeO_2-ZrO_2-TeF_4 system.

The 2h glass-ceramic sample that includes a mixture of amorphous-like and crystalline phases (the novel crystalline phase and $ZrTe_3O_8$ respectively) forms a more random assemblage of crystal shapes (Figure 6). Especially, this glass-ceramic material exhibits a multiscale microstructure: some ~200 nm anti-glass phases are embedded in the residual glassy phase which partially crystallizes the ~ 20 nm $ZrTe_3O_8$ cubic phase. As previously shown by thermal analysis of both bulk samples and powders, bulk crystallization plays a major role upon heating of the $65TeO_2$-$35ZrF_4$ glass.

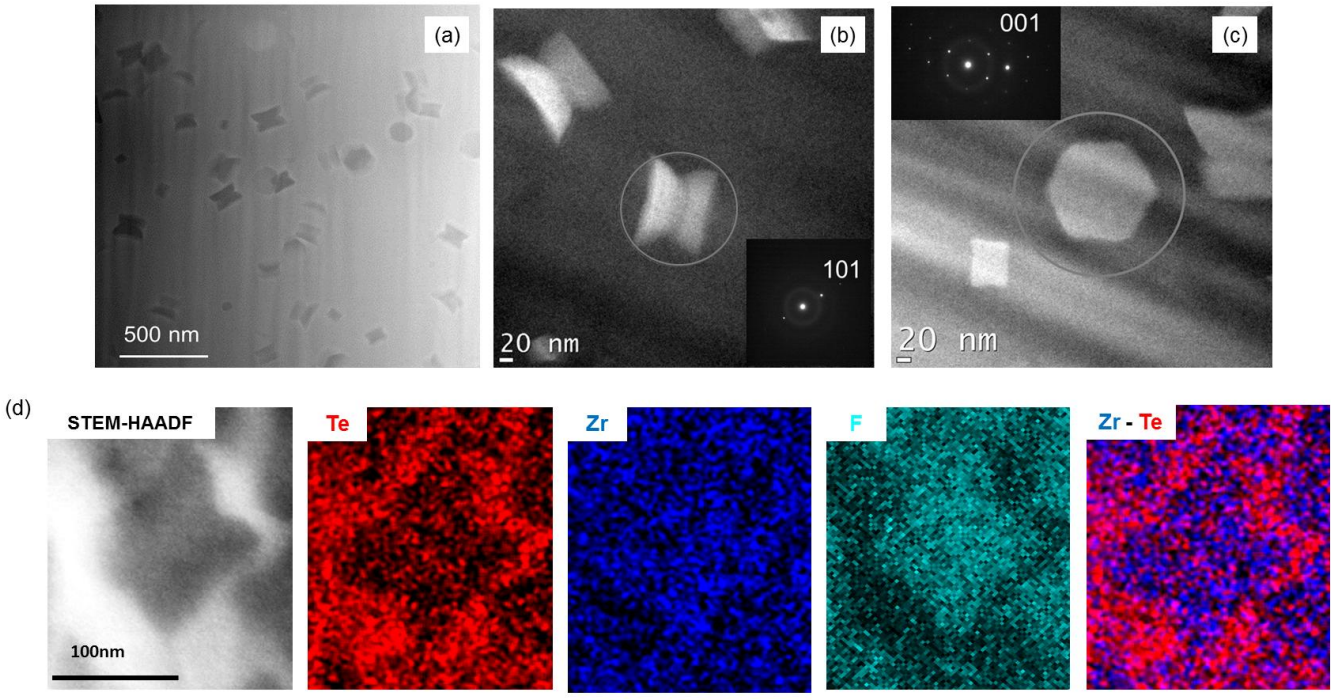

Figure 5: (a) STEM-HAADF images of glass-ceramic (1h30, 340°C), (b) and (c) BF and SAED (inset) patterns of crystals, (d) EDX-STEM (Te, Zr) and EFTEM (F) maps

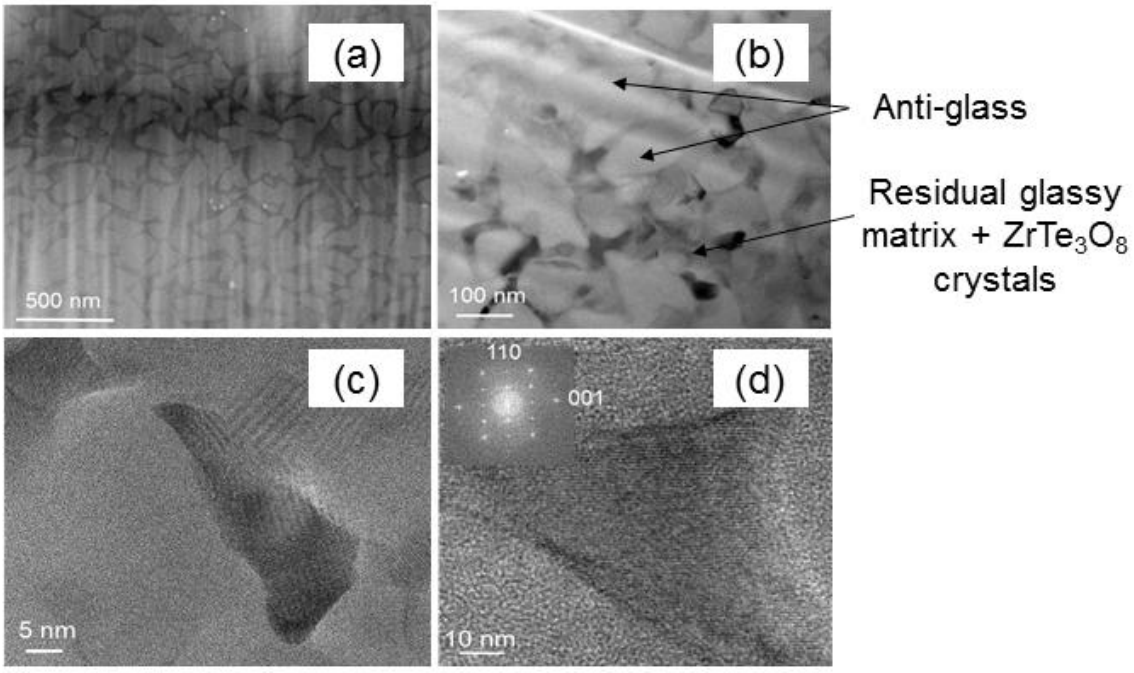

Figure 6: (a) and (b) STEM-HAADF images of glass-ceramic (2h, 340°C), (c) and (d) HRTEM and SAED (inset) patterns of $ZrTe_3O_8$ crystals

The evolution of the atomic local environments leading to the stabilization of the novel anti-glass phase was also studied by ^{125}Te and ^{19}F magic angle spinning (MAS) NMR spectroscopy. As shown in Figure 7(a), the ^{125}Te MAS spectrum of the $65TeO_2$-$35ZrF_4$ glass exhibits a broad isotropic resonance centered at 1620 ppm with an intense spinning sideband pattern due to a ^{125}Te chemical shift anisotropy of about δ_{csa} ~ -700 ppm and η_{csa} ~ 0.3. These values are close to those reported for TeO_4 units.[35] The ^{125}Te spectrum recorded using cross-polarization (CP) from ^{19}F is similar to that obtained from direct ^{125}Te excitation, indicating that F atoms are also in the vicinity of Te ones. The observed ^{125}Te resonance is thus assigned to pyramidal TeO_4-based oxyfluoride units. The ^{125}Te MAS spectra of the glass-ceramics are more complex. For the sample heat-treated for 1h30 at 340°C, a broader distribution of ^{125}Te isotropic shift is observed associated to the presence of both the glass and anti-glass phases. In addition to these signals, the ^{125}Te MAS spectrum of the glass-ceramic heat-treated for 2h at

340°C contains a much narrower spinning sideband pattern (δ_{iso} = 1490 ppm) which is filtered out from the ^{125}Te-{^{19}F} CPMAS spectrum (Figure 7a) and is obviously assigned to the $ZrTe_3O_8$ crystalline phase. Overall, these spectra show that the anti-glass crystalline phase ($Zr_{10}Te_9O_xF_y$), as determined by EDX measurements is associated to a broad distribution of ^{125}Te isotropic shift close to that observed for the glass, but with a lower average position (δ_{iso} ~ 1530 ppm) reflecting an increased number of F atoms in the Te coordination sphere in agreement with its composition (Figure 5d).

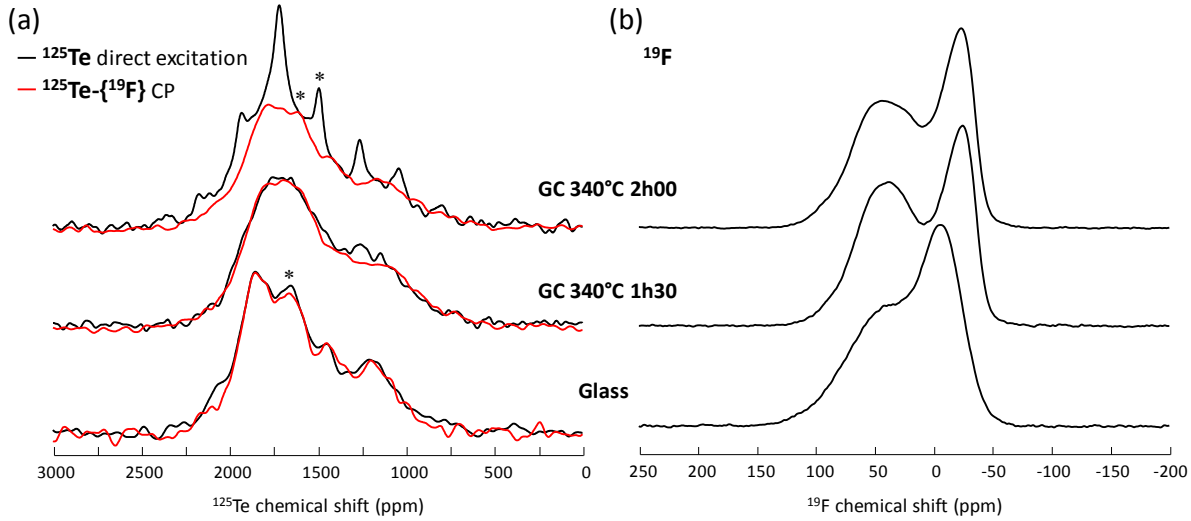

Figure 7: (a) Quantitative ^{125}Te spin-echo MAS (black lines) and ^{125}Te-{^{19}F} cross-polarization spin-echo MAS (red lines) NMR spectra recorded at a spinning rate of 14.285 kHz. The ^{125}Te isotropic chemical shifts are indicated by asterisks. (b) Quantitative ^{19}F spin-echo MAS spectra of the glass and glass-ceramics samples recorded at a spinning rate of 60.0 kHz. In (a, b) Spectra of the glass and of the glass-ceramics (GC) heat-treated at 340°C for 1h30 and 2h are shown from bottom to top.

The presence of local disorder in the metastable anti-glass phase is also revealed by ^{19}F NMR. As shown in Figure 7(b), the ^{19}F MAS spectrum of the $65TeO_2$-$35ZrF_4$ glass recorded at very fast spinning rate displays two isotropic resonances centered at 40 and -8 ppm with broad

linewidths (FWHM of 75 and 40 ppm, respectively) associated to large distributions of these two types of F environments. For the glass-ceramic samples, a decrease of the ^{19}F average isotropic shift of the most-shielded contribution toward -25 ppm is only observed without the appearance of additional narrow resonances, indicating that large distributions of the fluorine environments are preserved during crystallization of the $Zr_{10}Te_9O_xF_y$ anti-glass phase (Figure 7b). Note that the ^{19}F isotropic shifts reported for the seven distinct F sites of crystalline ZrF_4 (ranging from 9.5 to 30.6 ppm) stand between the positions of the two broad lines observed for the glass and glass-ceramic samples making their assignment difficult.[36] Therefore ^{19}F-{^{125}Te} and ^{19}F-{^{91}Zr} double-resonance MAS experiments were performed to assign these two broad peaks. Figure 8(a) shows a comparison between ^{19}F-{^{125}Te} 1D HSQC MAS spectra selectively probing F atoms in the vicinity of Te ones and ^{19}F reference spin-echo spectra recorded with equivalent echo duration. This immediately reveals that the contribution at 40 ppm is associated to F atoms bonded to Te, while the most-shielded line which is almost filtered-out from the ^{19}F-{^{125}Te} HSQC spectra corresponds to F atoms at remote distances from Te. Similarly, the comparison between ^{19}F spin-echo reference spectra and their differences with ^{19}F {^{91}Zr}-dephased ones (Figure 7b) demonstrate that this most-shielded line is associated to F atoms in the vicinity of Zr ones, while the line at about 40 ppm with a weaker {^{91}Zr}-dephasing effect corresponds to F atoms with a lower coordination to zirconium. Accordingly, the most-shielded line is assigned to F atoms bridging Zr polyhedra ($F_{Zr,Zr}$) while the one at 40 ppm is assigned to fluorine bonded to both Zr and Te atoms ($F_{Zr,Te}$). This suggests a non-random distribution of fluorine in the glass and in the anti-glass network, Te-F-Te bond being unfavorable.

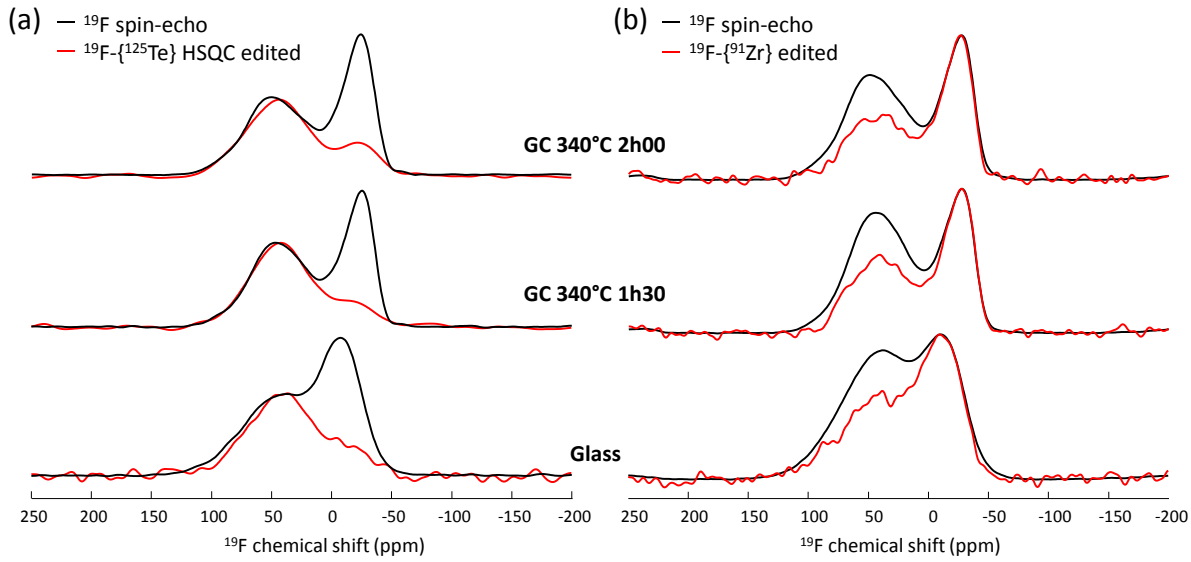

Figure 8: (a) ^{19}F-{^{125}Te} HSQC MAS spectra (red) and ^{19}F spin-echo MAS (black) spectra recorded at a spinning rate of 60 kHz with equivalent echo duration. (b) ^{19}F spin-echo (black) spectra and their differences (red) with {^{91}Zr}-dephased spin-echo spectra obtained at a spinning rate of 50kHz. Spectra of the glass and of the glass-ceramics (GC) heat-treated at 340°C for 1h30 and 2h are shown from bottom to top, respectively.

The relative amount of F atoms involved in Zr-F-Zr linkages determined from fits of the ^{19}F quantitative spectra roughly increases from 36% in the glass up to 43% in the glass-ceramic heat-treated at 340°C for 2h, which is consistent with a larger content of F and Zr in the anti-glass phase relative to that of the initial glass (counterbalanced by the crystallization of $ZrTe_3O_8$). As also observed in ^{19}F-{^{125}Te} 2D HSQC spectra (Figure 9a), the average long-range ordering taking place in the anti-glass phase is mainly revealed as a shift (~ -17 ppm) of the $F_{Zr,Zr}$ line and the appearance of asymmetrical distributions of ^{19}F and ^{125}Te isotropic chemical shifts which nevertheless remains almost similarly broad as those of the glass. To further probe short-range fluorine proximities, 2D ^{19}F-^{19}F dipolar double-quantum correlation MAS experiments were used. As shown in Figure 9(b), the ^{19}F-^{19}F dipolar correlation spectrum of the glass displays an intense $F_{Zr,Zr}$ auto-correlation peak in addition to cross-

correlations between the $F_{Zr,Zr}$ and $F_{Zr,Te}$ lines, while no $F_{Zr,Te}$ auto-correlation is observed. This reflects again the affinity of fluorine to coordinate Zr and suggests the association of F-rich Zr polyhedra with O-rich $TeO_{4-x}F_x$ units within the glass network.

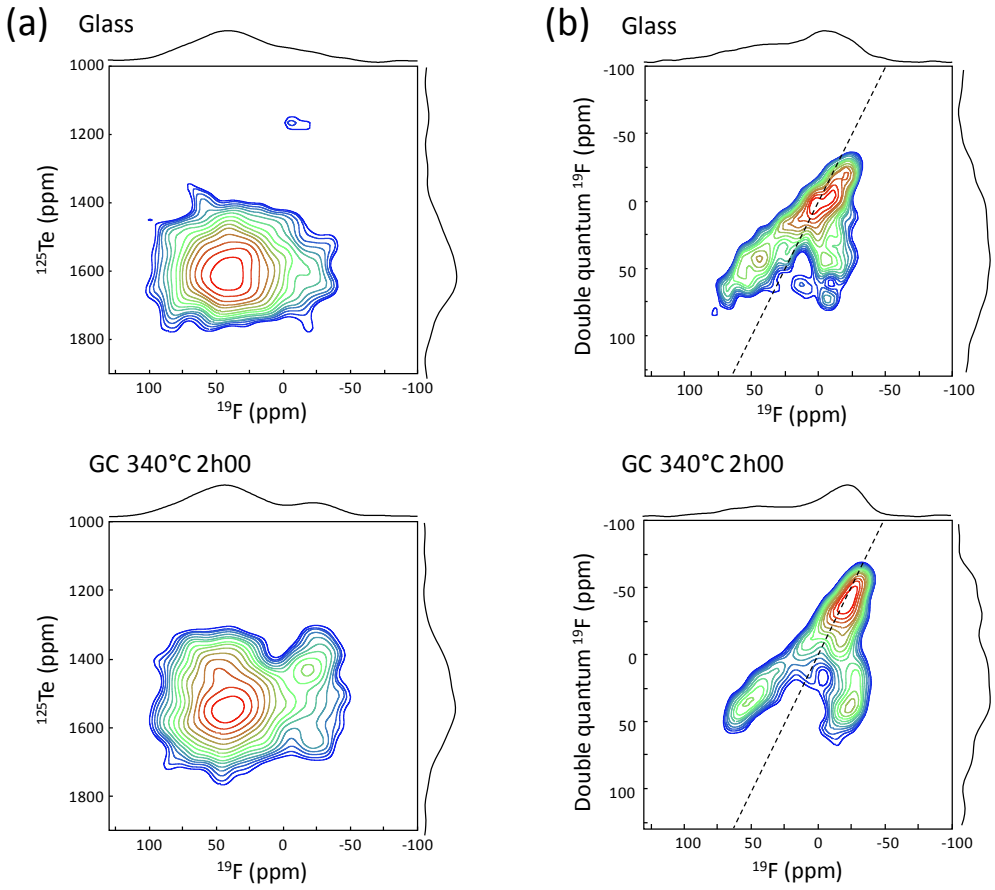

Figure 9: (a) ^{19}F-{^{125}Te} 2D HSQC MAS (60 kHz) spectra and (b) 2D ^{19}F homonuclear dipolar double-quantum correlation MAS (50kHz) spectra of the glass (top) and the glass-ceramic heat-treated at 340 °C for 2h (bottom).

The 2D spectrum of the glass-ceramic heat-treated for 2h displays the same F-F correlation pattern indicating a similar ordering amongst $F_{Zr,Zr}$ and $F_{Zr,Te}$ sites with ^{19}F isotropic chemical shift distributions nearly as wide as those of the glass. All these observations reveal the peculiar nature of the novel anti-glass phase which displays long-range averaged cationic ordering, preferential Zr-F and Te-O bonds, and retains wide distributions of local

environments (bond-lengths and angles, next-nearest second neighbors) very similar to that of the parent glass.

Characterizations of glass-ceramics. *b. Optical transmission, ellipsometry and luminescence properties.*

The optical transmission was measured for all glass and glass-ceramic Tm^{3+}-doped samples and the corresponding data are graphed in Figure 10(a). One can evidence very easily the specific absorption bands related to the incorporation of Tm^{3+} ions and as well observe that the measured data reproduce rather well the qualitative aspect provided by the pictures of undoped samples and displayed in Figure 10(b). Moreover, two different stages can be clearly identified. Indeed, up to 1h30 of heat-treatment, the produced glass-ceramics remain rather transparent in the visible (even highly transparent for the 1h heat treated sample), whereas the samples fabricated with a heat-treatment duration equal to 2h and beyond become completely opaque (or almost) to visible light. This can be explained by the similar refractive index of both the glass matrix and the new anti-glass phase, as testified by the ellipsometry measurements (a difference of only 8.10^{-3} was evaluated between the glass and the 1h glass-ceramic samples - see Table 1). As well, beyond 2h of heat treatment, with the appearance of the $ZrTe_3O_8$ phase, the optical transmission in the visible is strongly degraded, suggesting this time that light scattering is much more pronounced. Again, ellipsometry measurements clearly reveal that the refractive index difference between the anti-glass and the $ZrTe_3O_8$ phases becomes now large (a difference of 3.10^{-2} was ascertained between the 1h and 2h glass-ceramic samples – see Table 1), provoking important birefringence effects.

Final comment on this part will finally focus on the NIR range, where it can be observed that the elaborated glass-ceramics remain highly transparent up to 2h of heat treatment (Figure 10(a)).

Parent glass	Glass-ceramic (GC) 1h 340°C	Glass-ceramic (GC) 2h 340°C
1.832	1.824	1.854

Table 1: Refractive indices measured for the glass and glass-ceramics (GC) samples heat-treated 1h and 2h at 340°C.

Besides, the absorption cross section σ_{abs} can be extracted from the optical transmission data, by using the following Beer-Lambert equation:

$$\sigma_{abs} = \frac{2.303}{N.l}.OD(\lambda),$$

where N corresponds to the density of Tm^{3+} ions (ions/cm^3) contained in the sample (such value is estimated from the experimental sample density measured by Archimedes' principle and from the measurement of the actual chemical composition), l is the thickness of the polished glass or glass-ceramics sample, and OD(λ) is the optical density value at the wavelength λ (here, λ = 792 nm represents the central wavelength of the absorption band of interest – Cf. 808 nm laser pump diode employed as the excitation source for the NIR PL measurements).

Calculated values are displayed in Figure 10(c): they range from ~ 7.0×10^{-21} to ~ 5.3×10^{-20} cm^2 (multiplication by a factor of ~ 7.5) which corresponds to typical values reported in the case of Tm^{3+}-doped tellurite samples.[37-40] Again, two stages can be identified: whereas the absorption cross-section remains roughly constant up to 1h30 of heat-treatment (see Figure 10(c)), the former starts increasing around 2h of heat-treatment and really takes off beyond that time (extremely clear for the 3h treated sample). This observation is unambiguously in

concordance with the appearance of the $ZrTe_3O_8$ phase, and directly underlines that some proportion of Tm^{3+} ions is incorporated within such phase.

Finally, it is noteworthy that the absorption provoked by OH groups (absorption band located around 3000 nm) has been strongly reduced, clearly proving the efficiency of fluorine addition, as it was already testified for instance in [ref 8].

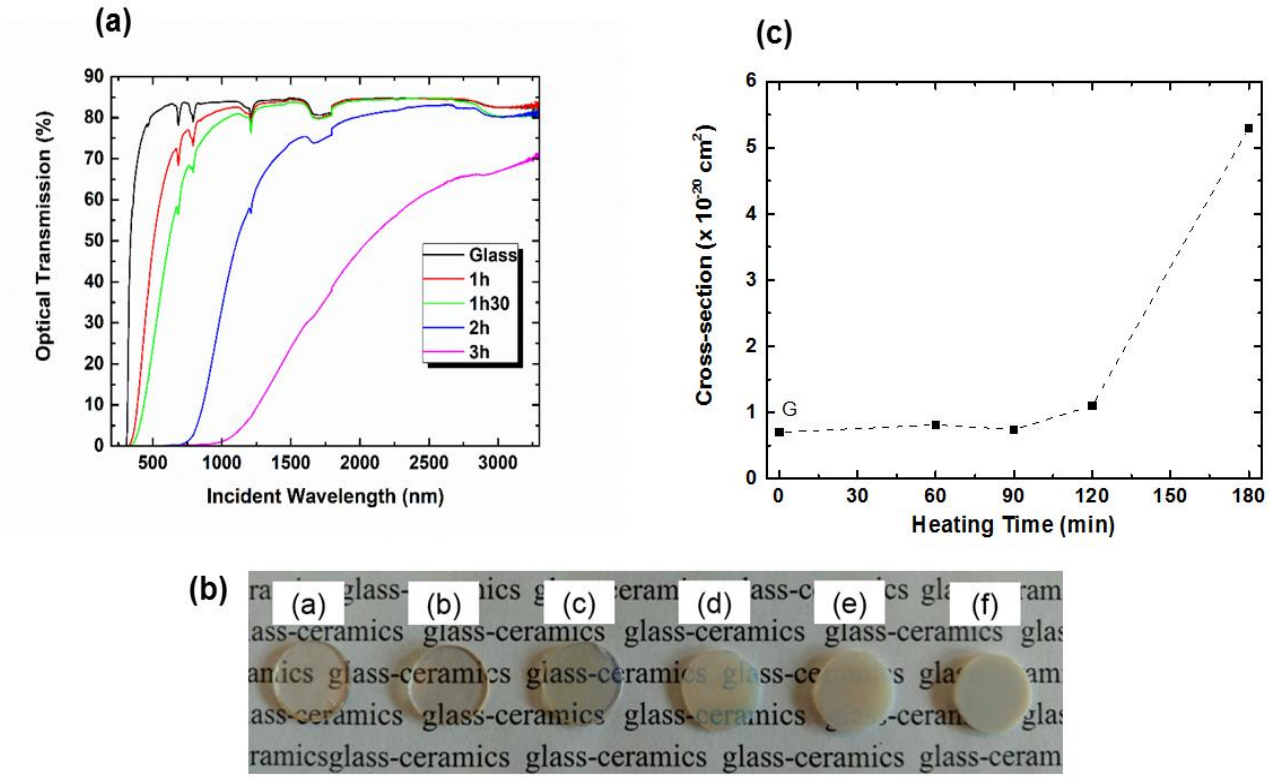

Figure 10: (a) Optical transmission data collected for the 1 at.% Tm^{3+}-doped $65TeO_2$-$35ZrF_4$ samples (thickness ~ 1 mm) and displayed in the full range (200 – 3300 nm). (b) Photographs of the undoped $65TeO_2$-$35ZrF_4$ composition: parent glass (a), glass-ceramics heat-treated at 340°C for 30 min (b), 1h (c), 1h30 (d), 2h (e) and 3h (f). (c) Evolution of the absorption cross-section at λ = 792 nm (transition $^3H_6 - {}^3H_4$), for the 1 at.% Tm^{3+}-doped $65TeO_2$-$35ZrF_4$ samples. Note that the G label stands for the glass sample.

Photoluminescence data

PL of Tm^{3+}-doped samples was also evaluated both in the visible and in the NIR ranges. Figure 11(a) represents the normalized PL intensity in the visible range (*$^3F_{2-3}$ – $^3H_6$ transition).*[41] Whereas strictly no modifications can be evidenced up to 1h30 of crystallization duration, the spectral shape clearly changes after 2h of heat-treatment and beyond: again, a clear separation exists around that pivotal heat-treatment time. The interpretation of such spectral differences observed in the PL spectra is however not straightforward, as the first simple explanation would be that rare-earth ions are not incorporated within the new anti-glass crystal phase, but manage to penetrate only the $ZrTe_3O_8$ crystal lattice. In fact, such interpretation of the PL data would be completely incorrect, and only the consideration of the structural (both NMR and Raman spectroscopy) data allows bringing some light to the current problem and drawing the correct conclusion. Indeed, as already shown in Figure 4, Raman spectra are almost identical after 1h30 of heat-treatment at 340°C, thus testifying to the crystallization of some « anti-glass » structure as previously discussed. The inherent sub-lattice anionic disorder (similar to what is encountered in a glass) then explains that the light emission of Tm^{3+} does not seem affected, even though rare-earth ions, from a statistical point of view, are most than likely inserted within the crystalline phase. Indeed, there is absolutely no physical explaining that Tm^{3+} ions would remain located only within the glassy matrix and would not be incorporated within the anti-glass crystal phase. On the other hand, the crystallization of the well-ordered $ZrTe_3O_8$ phase leads unambiguously to the appearance of additional features (Figure 11(a)), correlated to modified crystal-field effects in the 2h and 3h heat-treated samples. Thus, Tm^{3+} ions definitely enters (at least partially) the crystal lattice of $ZrTe_3O_8$, likely in substitution of Zr^{4+} ions. In the end, such modification of the Tm^{3+} environment occurring between 1h30 and 2h of heat treatment is also at the origin of the consequent variation of the absorption cross-section at 792 nm, as mentioned above.

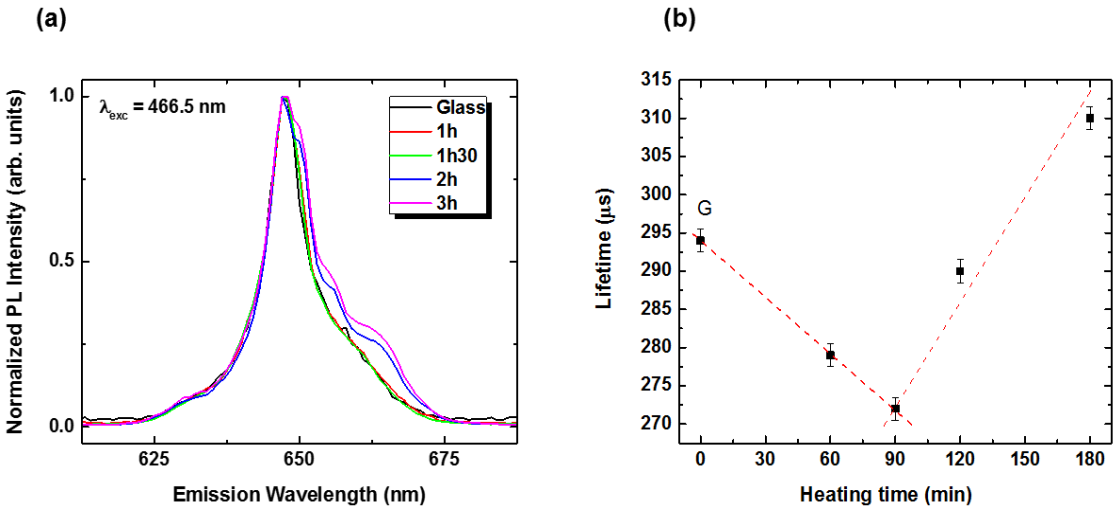

Figure 11: (a) Normalized PL intensity ($^3F_{2\text{-}3} - {}^3H_6$ transition) collected for the 1 at.% Tm^{3+}-doped $65TeO_2$-$35ZrF_4$ samples, for λ_{exc} = 466.5 nm. (b) Corresponding lifetime values measured as a function of the heat-treatment duration (note that the G label stands for the initial glass and that the dashed lines serve there only as guides for the eyes).

Figure 11(b) shows the evolution of the lifetime ($^3F_2$,$^3F_3$ – $^3H_6$ transition) versus the heat-treatment time. Here again, the graph can be separated in two different stages: up to 1h30 and beyond. Over the first stage, the lifetime value (extracted from almost single exponential PL decay curves – not shown here) drops from 294 to 272 µs (-7.5 %), and then increases again above 310 µs (+14 %). Again, such behaviour highlights the difference between samples produced for heat-treatments shorter or equal to 1h30, with those fabricated for longer times. The evolution of the lifetime value beyond 1h30 is easily understandable. Indeed, as it was demonstrated that some proportion of Tm^{3+} ions do enter the well-ordered $ZrTe_3O_8$ crystal phase (cf. Figure 11(a)), it is expected that the associated lifetime will simultaneously increase thanks to the improvement of the overall crystalline quality. For shorter times, the formation of the new anti-glass crystal phase (showing some structural disorder, similar to that encountered in the glass) leads to the moderate reduction of the lifetime. At first glance, such

evolution could appear somehow surprising but is probably connected to the slightly different chemical compositions highlighted in the STEM-EDX analysis (Figure 5). Indeed, the latter clearly revealed fluorine richer anti-glass nanocrystals embedded in a fluorine impoverished glass matrix. The next step is then to understand that Tm^{3+} ions are likely to be randomly distributed within the glass-ceramic, and that the volumic fraction of the glassy matrix remains larger than that occupied by the anti-glass nanocrystals. Finally, in comparison with oxide materials, fluorides are well-known to represent ideal host matrices for the incorporation of rare-earth ions, hence leading to longer lifetime values.[42] Thus, the direct consequence of all this will be the slight reduction of the average lifetime value.

Another aspect of this work is related to the light emission in the NIR range. In particular, Tm^{3+} ions are mostly attractive for their NIR emission around 1.8-2 µm, corresponding to the $^3F_4$-$^3H_6$ transition.[37-40] Figure 12 (a-b) plots the evolution of the NIR corrected PL intensity (and of the corresponding integrated intensity) as a function of the heat-treatment time. One can see that the emitted intensity is more or less constant while switching from the glass to the glass-ceramic sample obtained after 1h30 of heat-treatments, and that beyond this time, it considerably takes off (for samples heat-treated 2h and 3h, the integrated intensity is respectively multiplied by factors larger than 3 and 5 – see Figure 12(b)). One of the main cause explaining such PL intensity increase beyond 1h30 of heat-treatment is the augmentation of the absorption cross-section of Tm^{3+} ions (Cf. Figure 10(c)), which is related to the concomitant partial transformation of the novel anti-glass disordered phase into the well-ordered $ZrTe_3O_8$ phase. Obviously, further and full interpretations of the PL intensity variation would require the calculation of the emission cross-section. And finally, it is also important to emphasize that the evolution of the PL intensity as a function of the heat-treatment time was also followed in the visible range (not shown here), and that it reveals exactly the same trend as the one observed for NIR data.

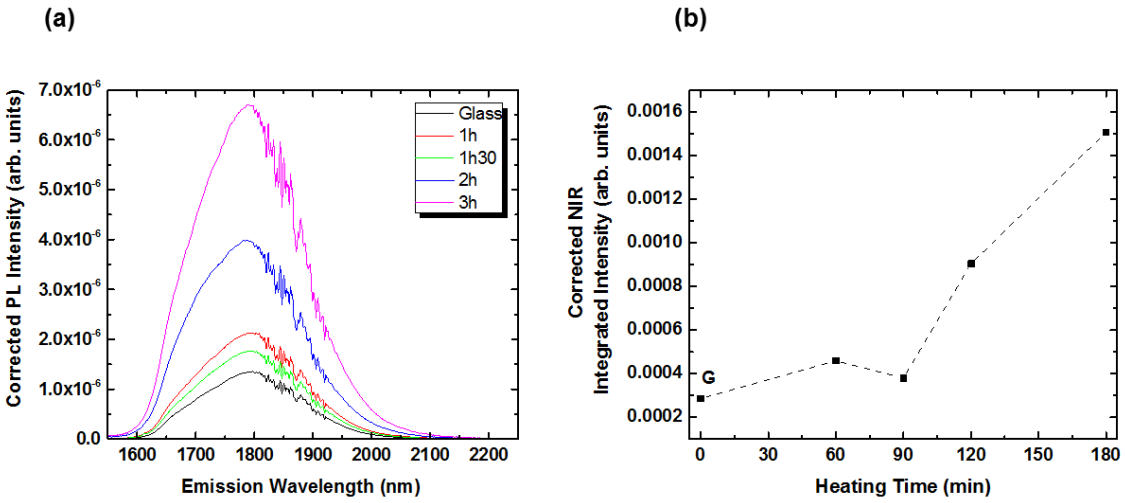

Figure 12: (a) NIR corrected PL intensity ($^3F_4$-$^3H_6$ transition) collected for different heat-treatment times. (b) Corresponding integrated intensity displayed as a function of the heat-treatment time. Note that the G label stands for the initial glass.

To summarize, all the properties (optical transmission and absorption, emitted PL) measured in this work clearly testify the different behaviour evidenced for the Tm^{3+}-doped samples produced before and after the appearance of the $ZrTe_3O_8$ crystal phase. In other words, the measured properties perfectly reflect the modifications occurring during the heat-treatment, and then, Tm^{3+} ions seem to act as an adequate structural probe, in a similar manner to what is well-known for the luminescence of Eu^{3+} rare-earth ions (as an illustration, see [43]).

Crystal structure.

Single crystals suitable for structural studies could be obtained in samples of various compositions and heat-treatments. They were prepared from compositions in the range $40ZrF_4$-$60TeO_2$ to $50ZrF_4$-$50TeO_2$. 2 g of stoichiometric compositions were melted at 800°C in a covered platinum crucible and quenched to room temperature or slowly cooled down to

600°C, 500°C or 400°C and then quenched in air in order to understand the order/disorder phenomena related to this new crystalline phase.

Depending on the nominal composition of the batches, the ratio Zr/Te of the resulting single crystals is in the range 1.3-1.6 according to EDX-SEM analysis (Table S1). These compositions are slightly different from the crystals composition in the glass-ceramic (ratio Zr/Te ~ 1.1) suggesting that the novel phase corresponds to a complex series of micro-phases rather than a stoichiometric compound. Their characterization on a 4-circle diffractometer allowed to identify the presence of known crystalline phases, even in small proportion, in these samples and to begin the structural study of the novel phase.

The pseudo-binary system ZrF_4-TeO_2 must be considered as a part of the quaternary system ZrF_4-ZrO_2-TeF_4-TeO_2 and phases belonging to the quaternary and to each of the other binary systems are likely to be present.[19] Indeed a few numbers of single crystals of α- and β-ZrF_4, various zirconium oxyfluorides, TeO_2 and/or $Te_2O_3F_2$ are identified as by-products in very small proportion, depending on the composition and thermal treatment.[44-47] In the samples containing close proportions of Zr and Te in the initial mixture heated during a short time (3-5 minutes) at 800°C, the X-ray powder pattern shows only the presence of the glass and the novel phase. The novel phase is present in great proportion as transparent thin platelets, often forming twins in "butterfly wings", as also observed by TEM. On the contrary, in the Te-rich samples, $ZrTe_3O_8$ crystallizes in great proportion with high size acicular single crystals.

The analysis of isolated single crystals of various initial bulk compositions by EDX-TEM (see Table S1) shows that their cationic composition is different from the initial mixture and richer in zirconium. The anionic composition is more difficult to determine because of the weak accuracy of EDX for light atoms. A strong deficit of negative charges is evidenced, showing that the number of O and F anions is likely underestimated by these analyses. Postulating arbitrarily that this underestimation is the same for O and F isoelectronic anions, a correction

has been performed in order to equilibrate the positive and negative charges. The resulting global formula for the novel phase grossly ranges between (Zr, Te)$(O,F)_{2.96}$ and (Zr, Te)$(O,F)_{2.77}$. It probably belongs to the pseudo-ternary ZrF_4-ZrO_2-TeO_2.

The examination of many single crystals of the novel phase has revealed a great structural complexity resulting from the formation of various long-range ordering superstructures depending on small changes of compositions and on temperature annealing conditions.

The basic structure, neglecting the superlattice reflections, has been investigated in parallel by the Rietveld method on a powdered sample of initial composition $45ZrF_4$-$55TeO_2$ heated 3 minutes at 800°C and quickly cooled to ambient temperature and on a single crystal extracted from a sample of initial composition $45ZrF_4$-$55TeO_2$ heated at 800°C and slowly cooled to ambient temperature. The substructure refined using single crystal data is hexagonal/trigonal with lattice parameters a = 3.981(1) Å, c = 4.107(1) Å. Solved and refined in the space group P-3m1 (see Tables 2, S2, S3 and Figure 13), it shows a strong analogy with α-UO_3 with the U site statistically occupied by Te and Zr cations and the anionic sites occupied by O/F anions.[48] In α-UO_3, the O1 site corresponds to the apices of an hexagonal bipyramid whose hexagonal basis is occupied by O2 anions. In $Te_{0.40}Zr_{0.60}O_{1.10}F_{1.80}$ (average composition of the crystal), the OF1 site is strictly identical to O1 site and also corresponds to the apices of the Zr/Te disordered cationic site. The OF2 site occupies the same basal position but seems only partly occupied. Moreover, a Fourier-difference map shows the presence of some residues of electronic density at the same z =0 level as the cation and OF1 sites, which can be refined in ½, -½, 0 with a partial occupation of the site called OF3. The anisotropic displacement parameters (Table S4) are positive/definite but rather high, in agreement with the statistical occupancy of the cationic site by cations Zr and Te presenting many crystallochemical differences in their anionic polyhedra. Because of the extensive disorder and the uncertainties on the ratio Zr/Te (which cannot be refined to avoid high correlations of the refined

parameters), the occupation rates of the anionic sites are very approximate and the structure refinement must only be considered as a limited approach of the true structure, related to the α-UO_3 type.

The analogy of the structure of the novel phase with α-UO_3 provides a first explanation of the presence of various superlattices deriving from this hexagonal/trigonal sublattice by multiplying the a and b parameters by 5, 7 or even more complex values and the c parameter by 3 or 5 (Figure S1). Indeed, a system of microphases of close composition is already known between UO_3 and U_3O_8 with a composition about $MO_{2.69-2.72}$ and orthorhombic unit cells deriving from the hexagonal unit cell of α-UO_3 by the relation: a = a(α-UO_3) * $\sqrt{3}$, b= m* a(α-UO_3), c = c(α-UO_3). A similar series of microphases is known in the ZrF_4-ZrO_2 system with compositions $Zr_3O_4F_4$, $Zr_7O_9F_{10}$ and $Zr_{10}O_{13}F_{14}$ and in the homologous system UF_4-ZrO_2.

The structure of these microphases can be described as an ordered creation of anionic vacancies in the O2 or OF2 site, changing some anionic hexagons to pentagons or even square faces. This behaviour allows to understand the structural role of OF3 site in $Te_{0.40}Zr_{0.60}O_{1.10}F_{1.80}$. which can correspond to the formation of pentagonal faces in the cationic plane, as shown in Figure 13.

On the powdered sample heated for 3 minutes at 800°C and quenched in air at room temperature, the refinement gives similar results as for the basic structure with a rather poor quality of refinement. No superlattice peaks are detectable but some anomalies appear for 00l peaks which are much narrower (FWHM ~ 0.094° and ~ 0.220° for 002 and 110 peaks respectively, see Figure S2) than the others which prevents to refine the structure with enough accuracy. A comparison with samples of various compositions heated at the same temperature during various durations shows that the 00l peaks are sometimes similar and sometimes narrower than the others. That is in apparent contradiction with the shape of the crystallites

which form very thin sheets perpendicularly to the [001] axis which should lead to hk0 reflections narrower than 001 ones. This discrepancy should rather likely correspond to the first step of the ordering process observed on the single crystal data and shows that the α-UO_3-type disordered phase is highly metastable and tends to long-range ordering after its recrystallization from the glassy matrix. This recrystallization process should begin by a lining up of the lone pairs of Te^{4+} polyhedral, forming sheets with weak bonds orientated perpendicularly to the 001 axis. Paradoxically, this fast process of reorientation of Te(O,F)nE polyhedral generates, in a first time, a great disorder in the hexagonal planes between Zr and Te polyhedral with cationic and anionic vacancies as observed in the α-UO_3 itself by neutron diffraction. Progressively, a long range ordering in orthorhombic microphases can develop between Te and Zr polyhedra, on the model of U_3O_8 and of the Zr-oxyfluorides, depending on the annealing time and temperature for compositions between $M(O,F)_{2.667}$ and $M(O,F)_3$.[49] In the first step of crystallization, the disorder inside the hexagonal planes prevents to determine if the unit cell is already orthorhombic as no real split of the reflections is detectable even at high angles, only a widening of some peaks being discernible.

A full structural study of the new series of ordered microphases in the Zr-Te-O-F system obtained by longer annealing time is out of the scope in the present study and will be the subject of further investigations.

Table 2.Crystal data and structure refinement.

Empirical formula	$Te_{0.40}\ Zr_{0.60}F_{1.80}O_{1.10}$
Formula weight (g/mol)	157.57
Temperature	293(2) K
Wavelength	0.7107 Å
Crystal system, space group	Trigonal, P -3 m 1
Unit cell dimensions	a = 3.9148(10) Å alpha = 90 deg. b = 3.9148(10) Å beta = 90 deg. c = 4.0432(10) Å gamma = 120 deg.
Volume	53.66(3) $Å^3$
Z, Calculated density	1, 4.876 Mg/m^3
Absorption coefficient	8.338 mm^{-1}
F(000)	70
Crystal size	0.03 x 0.03 x 0.005 mm
Theta range for data collection	5.042 to 27.439 deg.
Limiting indices	-5<=h<=5, -4<=k<=3, -5<=l<=5
Reflections collected / unique	327 / 62 [R(int) = 0.034]
Completeness to theta = 25.241	98.0 %
Refinement method	Full-matrix least-squares on F^2
Data / restraints / parameters	62 / 0 / 11
Goodness-of-fit on F^2	1.116
Final R indices [I>2sigma(I)]	R1 = 0.0306, wR2 = 0.0685
R indices (all data)	R1 = 0.0306, wR2 = 0.0685
Extinction coefficient	0.23(6)
Largest diff. peak and hole	0.696 and -0.630 $e.Å^{-3}$

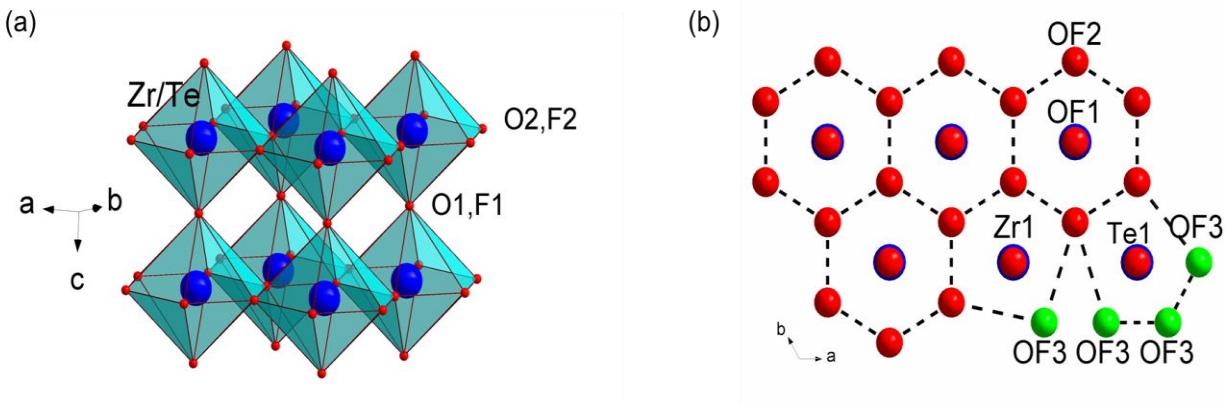

Figure 13: (a) Perspective view of the average structure of Zr,Te(O,F)x refined in the P-3m1 space group (α-UO_3 type) with one mixed Zr/Te site and two anionic sites OF1 and OF2, (b) Cationic and anionic planes at z=0. of the novel phase Zr,Te(O,F)x showing the coexistence of hexagonal and pentagonal anionic faces incorporating OF3 sites.

Conclusion

A novel $Zr_{10}Te_8O_xF_y$ anti-glass phase, deriving from the UO_3 structure, has been evidenced in a glass-ceramic with the nominal composition $65TeO_2$-$35ZrF_4$. The nano-crystals exhibit "butterfly wings" microstructure and lead to highly transparent glass-ceramics in the near infrared range. NMR studies revealed that the peculiar nature of the novel anti-glass phase which displays long-range averaged cationic ordering, shows preferential Zr-F and Te-O bonds and retains wide distributions of local environments, very similar to that of the parent glass. Longer heat-treatments or heat-treatments at higher temperature do not lead to the ordering of the novel phase but instead, the well-known $ZrTe_3O_8$ cubic phase crystallizes in the matrix. Upon doping, the Tm^{3+} ions act as an adequate structural probe since a change in photoluminescence is observed when the cubic $ZrTe_3O_8$ crystallizes in the matrix. Interestingly, single crystals with similar composition to the anti-glass phase could be

synthesized by slow cooling rates and some superlattices have been evidenced by single-crystal diffraction. The metastable anti-glass phase can thus be seen as a boundary that can allow understanding the crossover between the structure of crystals and that of disordered materials.

Acknowledgements

This work has been financially supported by the ANR "Investissements d'avenir" program TEMPOS (ANR-10-EQPX-50). The authors also acknowledge the French CNRS (FR3507) METSA network and more particularly, D. Pelloquin (CRISMAT, Caen, France).

Author Information

Corresponding author

*Email for G.D.: gaelle.delaizir@unilim.fr

ORCID

Gaëlle Delaizir: 0000-0002-6502-3938

Notes

The authors declare no competing financial interest.

References

(1) R. A. H. El-Mallawany, Tellurite Glasses Handbook: Physical Properties and Data 2002 CRC Press

(2) J. S. Wang, D. P. Machewirth, F. Wu, E. Snitzer, and E. M. Vogel, "Neodymium-doped tellurite single-mode fiber laser", Optics Letters, 19 (1994) 1448-1449

(3) Y. Tsang, B. Richards, D. Binks, J. Lousteau, A. Jha, "Tm^{3+}/Ho^{3+} codoped tellurite fiber laser", Optics Letters, 33 (2008) 1282-1284

(4) C. Dunn, F. Kong, G. Gu, T. W. Hawkins, M. Jonas, J. Parsons, A. Runnion, M. T. Kalichevsky-Dong, R. Salem, D. Liu, D. Gardner, P. Fendel, R. Synowicki, E. Cheung, J. T. Gomes, L. Lavoute, D. Gaponov, S. Février, L. Dong, "Solid tellurite optical fiber based on stack-and-draw method for mid-infrared supercontinuum generation", Fibers, 5 (2017) 37-48

(5) D. Rhonehouse, J. Zong, D. Nguyen, R. Thapa, K. Wiersma, C. Smith, A. Chavez-Pirson, "Low loss, wide transparency, robust tellurite glass fibers for mid-IR (2–5 μm) applications" Proc. SPIE (2013) 8898, 88980D

(6) K. Katarzyna, A. Tonello, B. M. Shalaby, M. Fabert, A. Barthélémy, G. Millot, S. Wabnitz, V. Couderc, "Spatial beam self-cleaning in multimode fiber"; Nature Photonics 11 (2017) 237-241

(7) E. A. Anashkina, A. V. Andrianov, V. V. Dorofeev, A. V. Kim, "Toward a mid-infrared femtosecond laser system with suspended-core tungstate–tellurite glass fibers", Appl. Opt. 55 (2016) 4522–4530

(8) I. Savelii, F. Desevedavy, J. Jules, G. Gadret, J. Fatome, B. Kibler, H. Kawashima, Y. Ohishi, F. Smektala, "Management of OH absorption in tellurite optical fibers and related supercontinuum generation" Opt. Mater. 35 (2013) 1595–1599

(9) T. Cheng, L. Zhang, X. Xue, D. Deng, T. Suzuki, Y. Ohishi, "Broadband cascaded four-wave mixing and supercontinuum generation in a tellurite microstructured optical fiber pumped at 2 μm", Opt. Express 23 (2015) 4125–4134

(10) C. Strutynski, J. Picot-Clémente, A. Lemière, P. Froidevaux, F. Désévédavy, G. Gadret, J. C. Jules, B. Kibler, F. Smektala, "Fabrication and characterization of step-index tellurite fibers with varying numerical aperture for near- and mid-infrared nonlinear optics", J. Opt. Soc. Am. B, 33 (2016) D12–D18

(11) S. Kedenburg, C. Strutynski, B. Kibler, P. Froidevaux, F. Désévédavy, G. Gadret, J. C. Jules, T. Steinle, F. Mörz, A. Steinmann, "High repetition rate mid-infrared supercontinuum generation from 1.3 to 5.3 μm in robust step-index tellurite fibers", J. Opt. Soc. Am. B, 34 (2017) 601–607

(12) T. Komatsu, H.G. Kim, H. Oishi, "New Transparent Nonlinear Optical Tellurite-Based Glass-Ceramics", Inorganic Materials 33 (1997) 1069-1074

(13) H. G. Kim, T. Komatsu, R. Sato, K. Matusita, "Crystallization of $LiNbO_3$ in Tellurite Glasses", Journal of Non-Crystalline Solids 162, (1993) 201-204

(14) A. De Pablos-Martin, A. Duran, M. J. Pascual, "Nanocrystallisation in oxyfluoride systems: mechanisms of crystallisation and photonic properties" Int Mater Rev, 57 (2012) 165–86

(15) L. L. Kukkonen, I. M. Reaney, D. Furniss, A. B. Seddon, "Nucleation and crystallisation behaviour of transparent, erbium III doped, oxyfluoride glass ceramics for active photonic devices" Phys Chem Glass, 42 (2001) 265–73

(16) C. Joshi, R. N. Rai, S. B. Rai, "Structural, thermal, and optical properties of Er^{3+}/Yb^{3+} co-doped oxyhalide tellurite glasses, glass-ceramics and ceramics", J Quant Spectrosc Radiat, 113 (2012) 397–404

(17) Z. X. Hou, Z. L. Xue, S. H. Wang, “Synthesis and spectroscopic properties of Er^{3+}-doped CaF_2 nanocrystals in transparent oxyfluoride tellurite glass-ceramics”, J Alloys Compd, 514 (2012) 109–112

(18) C. Yu, J. Zhang, L. Wen, Z. Jiang, “ New transparent Er^{3+}-doped oxyfluoride tellurite glass ceramic with improved near infrared and up-conversion fluorescence properties” Mater Lett, 61 (2007) 3644–6

(19) A. Ider, J.P. Laval, B. Frit, J. Carre, J.P. Bastide, "Etude du système TeO_2-TeF_4. Caractérisation structurale et thermique", Thermochimica Acta, 258 (1995) 117-124

(20) A. Hayashi, K. Noi, A. Sakuda, M. Tatsumisago, ”Superionic glass-ceramic electrolytes for room-temperature rechargeable sodium batteries” Nat. Commun. 3 (2012) 1–5

(21) F. Mizuno, A. Hayashi, K. Tadanaga, M. Tatsumisago, “New, highly ion-conductive crystals precipitated from Li_2S-P_2S_5 glasses” Adv. Mater. 17 (2005) 918–921

(22) J. B. Vaney, J. Carreaud, A. Piarristeguy, C. Morin, G. Delaizir, R. Viennois, M. Colas, J. Cornette, E. Alleno, J. Monnier, M. Bigot, A. Pereira Gonçalves, E. Branco Lopes, G. J. Cuello, V. Nassif, C. Candolfi, B. Lenoir, A. Pradel, “Stabilization of Metastable Thermoelectric Crystalline Phases by Tuning the Glass Composition in the Cu–As–Te System”, Inorg. Chem., 57 (2018) 754–767

(23) H. G Burckhardt, M. Trömel, “Strontium-undecaoxotellurat, $SrTe_5O_{11}$, eine CaF_2-Defektstruktur und ihre Beziehung zur Struktur einfacher Gläser”, Acta Cryst. C, C39 (1983) 1322-1323

(24) M. Trömel, W. Hützler, E. Münch, “Anti-glass phases and other lanthanide tellurates with fluorite-related structures”, Journal of the Less Common Metals, 110 (1985) 421-424

(25) M. Trömel, E. Münch, G. Blasse, G.J. Dirksen, "Formation and luminescence of lower symmetrical tellurite anti-glass phases", Journal of Solid State Chemistry, 76 (1988) 345-354

(26) O. Masson, P. Thomas, O. Durand, T. Hansen, J. C. Champarnaud, D. Mercurio, "On the structure of the disordered $Bi_2Te_4O_{11}$ phase", Journal of Solid State Chemistry, 177 (2004) 2158-2176

(27) A. Bertrand, J. Carreaud, G. Delaizir, M. Shimoda, J. R. Duclère, M. Colas, M. Belleil, J. Cornette, T. Hayakawa, C. Genevois, E. Veron, M. Allix, S. Chenu, F. Brisset, P. Thomas "New transparent glass-ceramics based on the crystallization of "anti-glass" spherulites in the Bi_2O_3-Nb_2O_5-TeO_2 system", Crystal Growth and Design, 15 (2015) 5086-5096

(28) A. Bertrand, J. Carreaud, S. Chenu, M. Allix, E. Véron, J.-R. Duclère, Y. Launay, T. Hayakawa, C. Genevois, F. Brisset, F. Célarié, P. Thomas, G. Delaizir, "Scalable and Formable Tellurite-Based Transparent Ceramics for Near Infrared Applications", Advanced Optical Materials, 4 (2016) 1482-1486

(29) G. Bodenhausen, D. J. Ruben, "Natural abundance of ^{15}N NMR by enhanced heteronuclear spectroscopy", Chemical Physics Letters, 69 (1980) 185-189

(30) M. Makrinich, E. Nimerovsky, A. Goldbourt, "Pushing the limit of NMR-based distance measurements – retrieving dipolar couplings to spins with extensively large quadrupolar frequencies", Solid State NMR, 92 (2018) 19-24

(31) Q. Wang, B. Hu, F. Fayon, J. Trébosc, C. Legein, O. Lafon, F. Deng, J. P. Amoureux, "Double-quantum 19F-19F dipolar recoupling at ultra-fast magic angle spinning NMR: Application to the assignment of ^{19}F spectra of inorganic fluorides", Phys. Chem. Chem. Phys., 11 (2009) 10391-10395

(32) V. Nazabal, S. Todoroki, A. Nukui, T. Matsumoto, S. Suehara, T. Hondo, T. Araki, S. Inoue, C. Rivero, T. Cardinal, "Oxyfluoride tellurite glasses doped by erbium: thermal analysis, structural organization and spectral properties", Journal of Non-Crystalline Solids, 325 (2003) 85-102

(33) T. Sekiya, N. Mochida, A. Soejima, "Raman spectra of binary tellurite glasses containing tri- or tetra-valent cations", Journal of Non-Crystalline Solids, 19i (1995) 115-123

(34) M. Koubaa, R. Karray , N. Dhifallah, A. Kabadou, L. Bsais, "Effect of manganese doping on vibrational and physical properties of $ZrTe_3O_8$", Journal of Alloys and Compounds, 709 (2017) 808-818

(35) M. N. Garaga, U. Werner-Zwanziger, J. W. Zwanziger, "^{125}Te NMR Probes of Tellurium Oxide Crystals: Shielding-Structure Correlations", Inorganic Chemistry, 57 (2018) 892-898

(36) C. Legein, F. Fayon, C. Martineau, M. Body, J.-Y. Buzaré, D. Massiot, E. Durand, A. Tressaud, A. Demourgues, O. Péron, B. Boulard, "^{19}F High Magnetic Field NMR Study of β-ZrF_4 and CeF_4: From Spectra Reconstruction to Correlation between Fluorine Sites and ^{19}F Isotropic Chemical Shifts", Inorganic Chemistry, 45 (2006) 10636-10641

(37) Y. P. Peng, X. Yuan, J. Zhang, L. Zhang, "The effect of La_2O_3 in Tm^{3+}-doped germanate-tellurite glasses for ~ 2 μm emission", Sci. Reports, 4 (2014) 5256

(38) R. Xu, Y. Tian, L. Hu, J. Zhang, "2 μm spectroscopic investigation of Tm^{3+}-doped tellurite glass fiber", J. Non Cryst. Solids, 357 (2011) 2489–2493

(39) J. Yuan, P. Xiao, "Compositional effects of Na_2O, GeO_2, and Bi_2O_3 on 1.8 μm spectroscopic properties of Tm3+ doped zinc tellurite glasses", J. Lumin., 196 (2018) 281–284

(40) H. Cankaya, A. T. Gorgulu, A. Kurt, A. Speghini, M. Bettinelli, A. Sennaroglu, “Comparative spectroscopic investigation of Tm^{3+}:tellurite glasses for 2-μm lasing applications”, Appl. Sci., 8 (2018) 333

(41) G. Ozen, B. Demirata, M. L. Ovecoglu, A. Genc, “Thermal and optical properties of Tm^{3+} doped tellurite glasses”, Spectrochimica Acta Part A, 57 (2001) 273–280

(42) R. Moncorgé, A. Braud, P. Camy, J. L. Doualan, “Fluoride laser crystals”, in Handbook of Solid-State Lasers, B. Denker and E. Shklovsky, Eds., 28-53 (2013)

(43) R. Jagannathan, M. Kottaisamy, “Eu^{3+} luminescence: A spectral probe in $M_5(PO_4)_3X$ apatites (M = Ca or Sr; X =F-, Cl-, Br- or OH-)”, J. Phys. Cond. Matter., 7 (1995) 8453-8466

(44) A. Ider, J.P. Laval, B. Frit, J. Carre, J.P. Bastide, "Crystal structure of $Te_2O_3F_2$", J. of Solid State Chem., 123 (1996) 68-72

(45) B. Holmberg, "Crystal structure of $Zr_7O_9F_{10}$", Acta Cryst., B26 (1970) 830-835

(46) R. Papiernik, B. Gaudreau, B. Frit, "Sur quelques oxyfluorures mixtes inédits de zirconium et d'uranium tétravalents", J. of Solid State Chem. 25 (1978) 143-156

(47) R. Papiernik, D. Mercurio, B. Frit, "Structure du tétrafluorure de zirconium, ZrF_4 α", Acta Cryst. B38 (1982) 2347–2353

(48) C. Greaves, B. E. F. Fender, “The Structure of a-UO_3 by Neutron and Electron Diffraction”, Acta Crystallographica, B28 (1972) 3609-3614

(49) F. Gronvold, Crystal Structure of Uranium Oxide (U_3O_8), Nature, 162 (1948) 70